Progress In Electromagnetics Research, Vol. 130, 493–512, 2012

GROUND MOVING TRAIN IMAGING BY KU-BAND RADAR WITH TWO RECEIVING CHANNELS

Y. Zhang*, W. Zhai, X. Zhang, X. Shi, X. Gu, and Y. Deng

The Key Laboratory of Microwave Remote Sensing, Chinese Academy of Sciences Center for Space Science and Applied Research, Chinese Academy of Sciences, Beijing 100190, China

Abstract—Radar imaging experiment of ground moving target — a light rail-way train by Ku-band radar with two receiving channels is introduced with imaging results presented. Both coherent and incoherent imaging as well as co-pol and cross-pol interferometric imaging were conducted with SAR amplitude images as well as interferometric-phase images obtained and compared. The along-track interferometric-phase images clearly show the speed variation of the train, i.e., the train traveled at an increasing speed in one direction and at a decreasing speed in the opposite direction. The incoherent imaging results indicate that for bistatic or multi-static radar imaging, the ultra-stable crystal oscillator (USCO) used by transmitter need not to be synchronized to the USCO used by receiver provided that the two basic crystal oscillators have small frequency difference and high stability. For better knowing the speed variation, Short Time Fourier Transform (STFT) is applied to the azimuthal signals to get the instant Doppler frequencies (IDFs), from which one can judge acceleration or deceleration status of the moving train. Electromagnetic scattering characteristics of the train are analyzed according to the SAR images. The estimated speed and length of the train are very well agreed with real situation.

1. INTRODUCTION

Ground moving target imaging by airborne or spaceborne synthetic aperture radar (SAR) [1–4] has been an interesting topic for a long time. Moving trains as usual ground moving targets have been imaged by many airborne or spaceborne SAR systems, but less imaged by

Received 2 June 2012, Accepted 20 July 2012, Scheduled 22 August 2012

* Corresponding author: Yunhua Zhang (zhangyunhua@mirslab.cn).

ground stationary radars. SAR system with two antennas and two receiving channels can be used both for three-dimensional topographic imaging if the antennas are installed across-track [5–7] and for ground moving target indication (GMTI) if the antennas are installed along-track [8, 9]. We conducted ground moving train imaging experiment with both Ku-band and Ka-band radar systems [10–12]. In [10, 11], we reported the high-resolution imaging results of a moving train. In [12], both coherent and incoherent interferometric SAR images of a moving train obtained by ground stationary two-channel Ku-band radar system were presented. Here, Coherent imaging means transmitter and receiver share the same ultra-stable crystal oscillator (USCO), and incoherent imaging means transmitter and receiver use two different USCOs. In the obtained amplitude images, the train doors and the connections between neighbouring compartments are imaged as strong point targets. Both coherent and incoherent interferometric-phase images show that the train traveled at a varying speed from north to south (south-bound) or from south to north (north-bound), and the speed variation of north-bound train was larger than that of south-bound train. In this paper, we extend the work and present more interferometric imaging results, i.e., cross-pol interferometries of HH-HV and VV-VH polarizations, as well as time-frequency analysis (TFA) results. We shall demonstrate that from the interferometric phase images one can easily judge the speed variation of the train although it could be very small. In order to further know how the speeds change for south-bound and north-bound trains, we perform TFA on the azimuthal signals to obtain the instant Doppler frequencies (IDFs) [13]. The IDFs can help us judge whether the train accelerates or decelerates very well. In [14] the fractional Fourier transform (FrFT) technique was used to estimate azimuthal Doppler parameters for better imaging.

The remainder of this paper is organized as follows. Section 2 briefly introduces the experimental radar hardware system. Section 3 introduces imaging model and data processing procedure. Section 4 presents imaging results and analyzes the electromagnetic scattering characteristics. Section 5 presents time-frequency analysis results on the azimuthal signals and Section 6 finally concludes the paper.

2. EXPERIMENTAL RADAR SYSTEM

The experimental radar system as shown in Figure 1(a) operates at Ku-band, including three standard-gain horn antennas (one is used for transmitting and connected to the transmitter, and the other two are used for receiving and they are connected to a two-channel

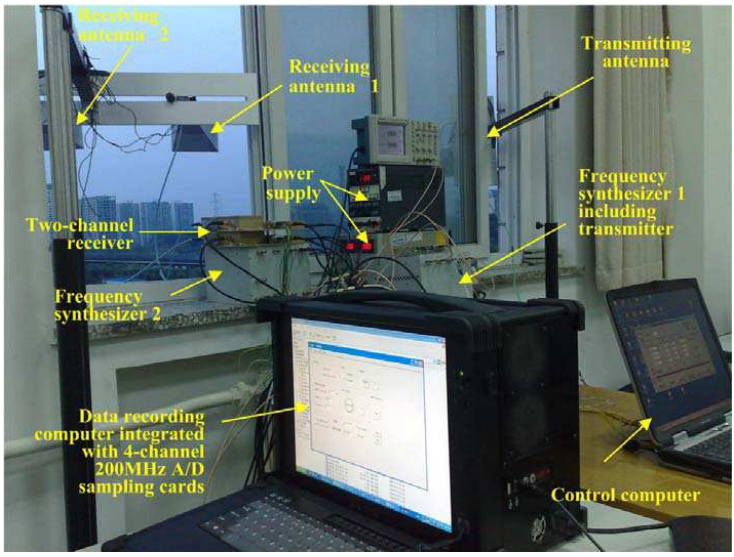

(a)

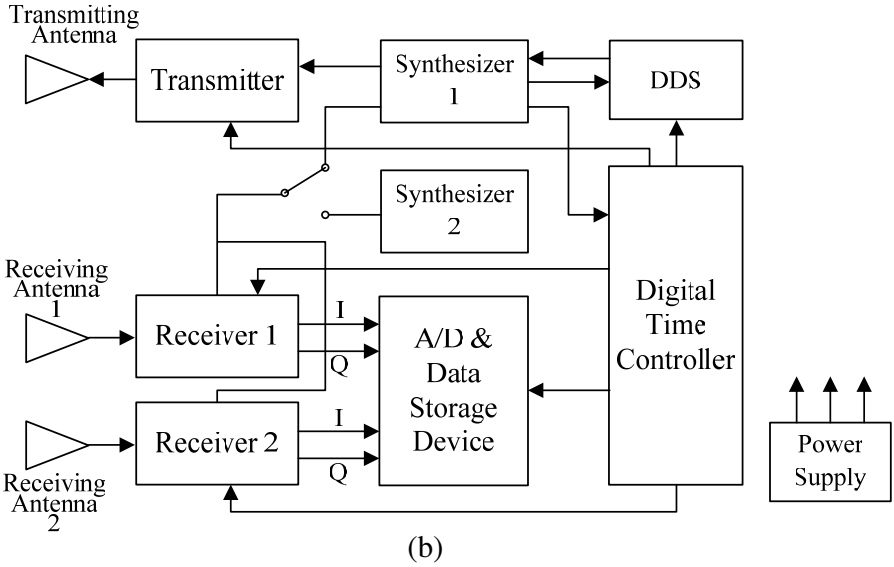

(b)

Figure 1. The configuration and diagram of the experimental radar system. (a) The configuration of experiment. (b) The radar diagram.

Table 1. Typical radar system parameters.

Parameters	Values
Central frequency	13.58 GHz
Frequency phase noise (all)	−100 dBc/Hz @1 KHz
Bandwidth	100 MHz
Pulse width	$1 \sim 40\,\mu s$
Output power flatness	< 0.5 dB
Out-band and harmonics suppression	> 50 dB
Transmitted power	20 dBm
Noise figure of two-channel receiver	5 dB
Amplitude fluctuation between two receiver channels	< 1 dB
Phase fluctuation between two receiver channels	$< 1.0^\circ$ (RMS)
I/Q amplitude imbalance	$< 3^\circ$
I/Q phase imbalance	< 0.25 dB
Receiver output voltage level	± 1.0 V
Antenna form and 3 dB Beamwidth	Standard-Gain Horn, 10°
PRF	Up to 6000 Hz
A/D sampling rate	200 MHz
Sampling precision	14 bit

receiver and separated by 0.4 m), two frequency synthesizers (these two synthesizers are referred to two different 100 MHz USCOs), two-channel receiver, transmitter (frequency up-converter + digital Chirp), controlling electronics, data recording devices. Figure 1(b) presents the diagram of the radar system, from which one can see that there are two frequency synthesizers, and the synthesizer 1 provides local frequencies for both transmitter and two-channel receiver, while the synthesizer 2 only provides local frequencies for two-channel receiver. In the radar system, the transmitter is composed of a frequency up-convertor and a solid-state power amplifier (SSPA). The "Digital Time Controller" unit acts as the central control electronics, i.e., it controls the transmitter, two-channel receiver and the data sampling and storage unit. The DDS (direct digital synthesizer) is a digital chirp signal generator which outputs digitally generated IF chirp signal. The "A/D & Data Storage Device" unit samples the echo data from two-channel

receiver and stores them for post processing. In the course of coherent interferometric imaging experiment, only synthesizer 1 was used, but in the course of incoherent interferometric imaging experiment, both synthesizer 1 and synthesizer 2 were used (the synthesizer 1 provided frequencies for transmitter and other units while the synthesizer 2 only provided frequencies for the two-channel receiver). The typical technical parameters are listed in Table 1.

3. IMAGING MODEL AND DATA PROCESSING

3.1. Imaging Model

The train of No. 13 light rail-way line in Beijing was chosen as the target, which passed by the experimental site (situated in the middle of two stations, the northern one is called "Wudaokou" station and the southern one is called "Zhichunlu" station). Figure 2 shows the skewed imaging geometry. The train traveled from left (north) to right (south) and from right (south) to left (north) now and then during experiment. The radar squint angle $\theta°$ was about 30° and the distance was about 150 m (in fact, these two parameters were estimated from data processing).

In the experiment, the radar was stationary while the target was moving; we easily assume inverse synthetic aperture radar (ISAR) [15] imaging model as a matter of course and apply ISAR processing to the experiment data. In fact, however, the ISAR imaging model is not applicable in this case because the train is too long that only part of compartments can be illuminated by the beams of the antennas due to

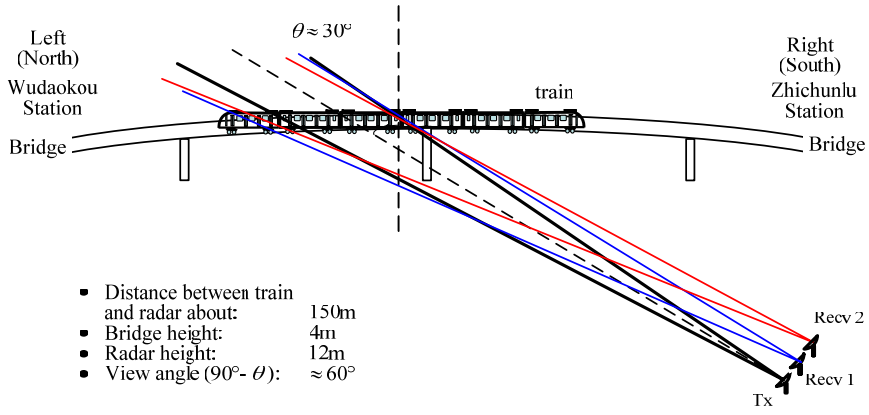

Figure 2. The geometry of the radar imaging experiment.

short observation distance. In ISAR imaging, the target is required to be entirely within radar beam and experiences a range of aspect angle change. In our experiment we can still utilize SAR imaging model by assuming the train was stationary while the radar was moving in an opposite direction relative to the moving direction of the train, but we did not know the speed, which should be estimated from data processing.

Different antennas were used for transmitting and receiving due to the short distance between the radar antennas and the target train. Although this is a bistatic imaging geometry, we still can treat it as monostatic imaging [16].

3.2. Data Processing

Data processing includes mainly eight steps as shown in Figure 3, i.e., raw data conversion, amplitude and phase correction of system response, antenna stability correction, background clutter removal, two-dimensional imaging and interferometric-phase image generation. Ordinary Range-Doppler (RD) [17, 18] imaging algorithm with range migration correction is used. In the following, we shall briefly explain the data processing procedure.

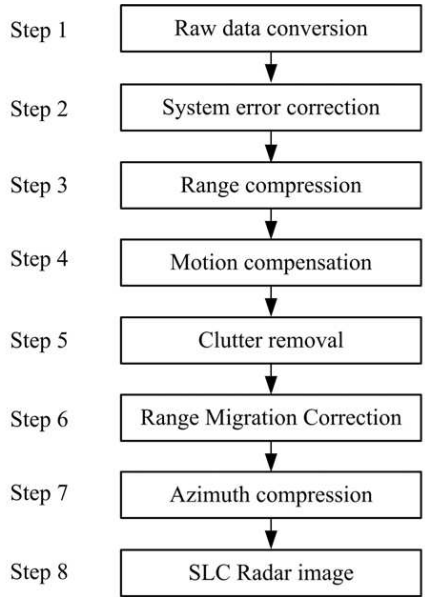

Figure 3. The data processing flow chart.

In step 1, raw data are organized into a two-dimensional matrix, $s(t,\ t_m)$, where t and t_m denote quick time and slow time, respectively.

In step 2, system amplitude and phase errors are corrected in frequency domain as follows,

$$S_1(f, t_m) = \mathrm{FFT}_t[s(t, t_m)]/A(f). \tag{1}$$

where $A(f)$ denotes system error function obtained through calibration operation.

In step 3, range compression is conducted:

$$s_2(t, t_m) = \mathrm{IFFT}_f\left[S_1(f, t_m) \cdot P_o^*(f)\right]. \tag{2}$$

where $P_o(f)$ is the FFT of the transmitted signal, and "*" denotes complex conjugate.

In step 4, motion compensation is conducted:

$$s_3(t, t_m) = s_2(t - \Delta t(t_m), t_m). \tag{3}$$

In step 5, clutter is removed:

$$s_4(t, t_m) = s_3(t, t_m) - \frac{1}{100}\sum_{i=1}^{100} s_3(t, t_m|_i). \tag{4}$$

In step 6, range migration is corrected:

$$s_5(t, t_m) = \mathrm{IFFT}_f\left\{\mathrm{FFT}_t[s_4(t, t_m)] \cdot \exp\left(-j4\pi\frac{Vt_m \sin\theta_0}{c} f\right)\right\}. \tag{5}$$

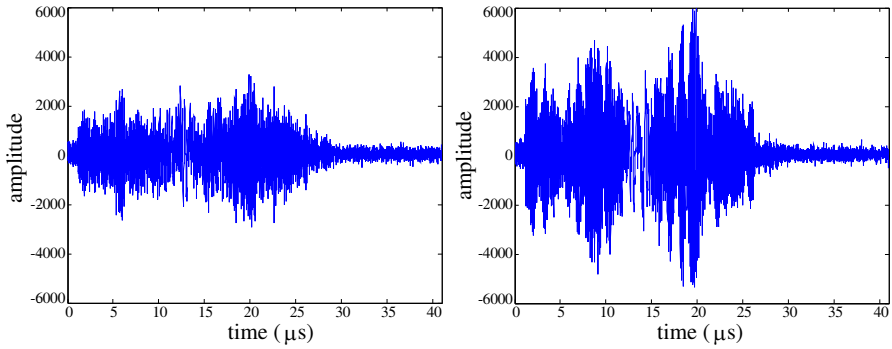

Figure 4. The radar echoes without and with train passing by. (a) Radar echo (I) without train passing by. (b) Radar echo (I) with train passing by.

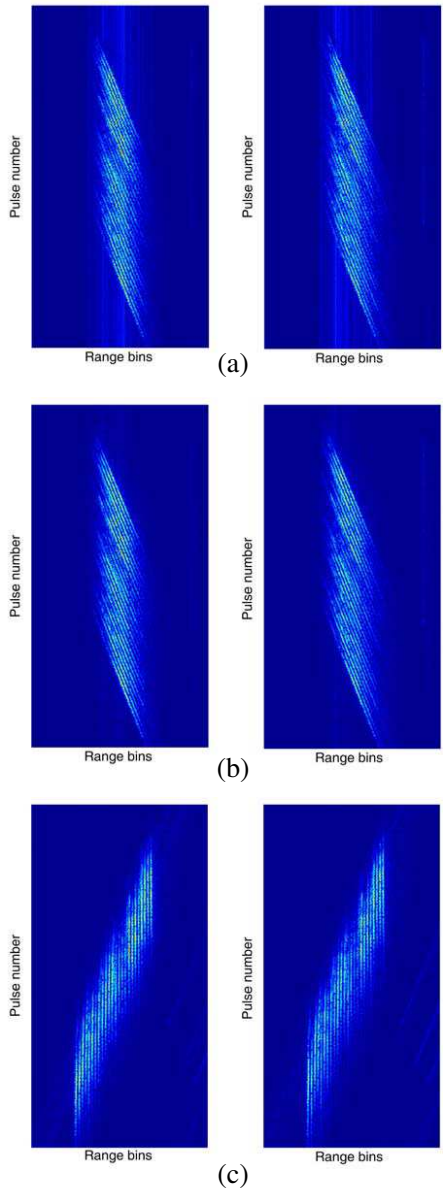

Figure 5. The obtained range profiles for a north-bound train (HH). Horizontal axis is for range bins and vertical axis is for pulse number (HH). (a) Range profiles before clutter removed. (b) Range profiles after clutter removed. (c) Range profiles after range migration corrected.

The train speed V and the viewing angle θ_0 of radar are related through the following expressions,

$$V = \sqrt{\left(\frac{\lambda f_{dc}}{2}\right)^2 - K_a \frac{\lambda R}{2}} \tag{6}$$

$$\theta_0 = \arcsin\left(\frac{\lambda f_{dc}}{2V}\right) \tag{7}$$

where f_{dc} and K_a are Doppler centroid and Doppler rate, respectively, and both of them can be estimated from echo data: the f_{dc} can be obtained by identifying the Doppler frequency center from the spectrum (i.e., the Fourier transformation) of the azimuthal signals while K_a can be obtained by dividing the spectrum width by the time (the product of PRF and the total pulse number covering the spectrum width). In our experiment, the width of obtained spectrum can be very well quantified. We must point out that the estimated K_a as above is just an initial estimation, it can be adjusted in a small range so as to get a much clear radar image.

In step 7, azimuthal compression is completed by matched filtering:

$$s_6(t, t_m) = \text{IFFT}\left\{\text{FFT}_{t_m}[s_5(t, t_m)] \cdot \text{FFT}_{t_m}\left[s_a^*(t_m)\right]\right\}. \tag{8}$$

where $s_a(t_m) = \exp(j2\pi f_{dc} t_m + j\pi K_a t_m^2)$.

Figures 4(a) and (b) show the radar echoes without and with a train, respectively. Figure 5 presents range profiles of the two channels after range compression without (a) and with clutter removed (b), as well as with range migration corrected (c). The presented echo data of Figures 4 and 5 are corresponding to a north-bound train.

In the course of imaging processing, the true train speed V and radar viewing angle θ_0 must be estimated by a joint searching scheme before getting the range migration correction done. Incorrect estimations will lead to unparallel range bins in respect to the vertical axis, and finally result in a defocused radar image and incorrect train length inferred from the image. In our experiment, we deduce from the experiment data that the average speed of the south-bound train is a slightly larger than that of the north-bound train, not only according to the estimated value but also from the plots of IDFs (will be shown in Section 5). The ambiguity number may exist in f_{dc} of (6) which should be first estimated so as to get correct Doppler frequency centroid, then (7) could be used to calculate the viewing angle. A good way for testing the accuracy of estimation is to compare the train length obtained from SAR image with that from reliable reference data. The estimated average speeds of the south-bound and the north-bound trains are about 18 m/s and 17.5 m/s, respectively, and the estimated

viewing angle is about 30°. By using these parameters, we get the train length of about 117.6 m from SAR image, which is very close to the true value: $2 \times 19.5 + 4 \times 19.0 + 0.6 \times 5 = 118$ m (the length of locomotive and compartment are 19.5 m and 19.0 m, respectively, and the length of connection between compartments is about 0.6 m). We should emphasize that autofocus algorithms [19–21] can be further used to improve the imaging quality on the basis of initially obtained images.

4. IMAGING RESULTS AND SCATTERING ANALYSIS

4.1. Imaging Results

In this section, we shall present amplitude images and interferometric-phase images for both coherent and incoherent imaging, as well as co-pol and cross-pol interferometric-phase images of coherent imaging.

Figures 6 and 7 present the obtained amplitude SAR images and interferometric-phase images corresponding to north-bound and south-bound trains in coherent and incoherent cases, respectively. Figures 6(a) and 6(b) show the two-channel SAR images obtained in coherent case for north-bound train and south-bound train, respectively, and Figure 6(c) shows their corresponding interferometric-phase images. The amplitude images indicate that there are 24 strong scattering centers. Figures 7(a) and 7(b) show the two-channel SAR images obtained in incoherent situation for north-bound train and south-bound train, respectively, and Figure 7(c) shows their corresponding interferometric-phase images. The amplitude images also indicate that there are 24 strong scattering centers as that shown in Figure 6.

By comparing Figures 6 and 7, one can see that incoherent imaging result is almost as clear as that of coherent imaging except for a little reduced signal to noise ratio (SNR), although the two 100 MHz USCOs used in two frequency synthesizers have a 47 Hz difference, both of them have a very good phase noise performance of as low as −155 dBc @ 1 kHz. It means that for bistatic or multi-static radar imaging, the USCOs used by transmitter need not to be synchronized to the USCO used by receiver provided that the two basic crystal oscillators have small frequency difference and high stability, because the frequency difference of the two USCOs leads to SNR loss in incoherent imaging.

The imaged scattering centers in the above amplitude SAR images are not aligned in a straight line as one expected. However, it is not strange after checking the targeted section of rail-way on the bridge where the train passed through, one can find that the bridge has a slight arch. Indeed, the slightly curved line formed by the imaged scattering centers just reflects the degree of the arch. If look into the

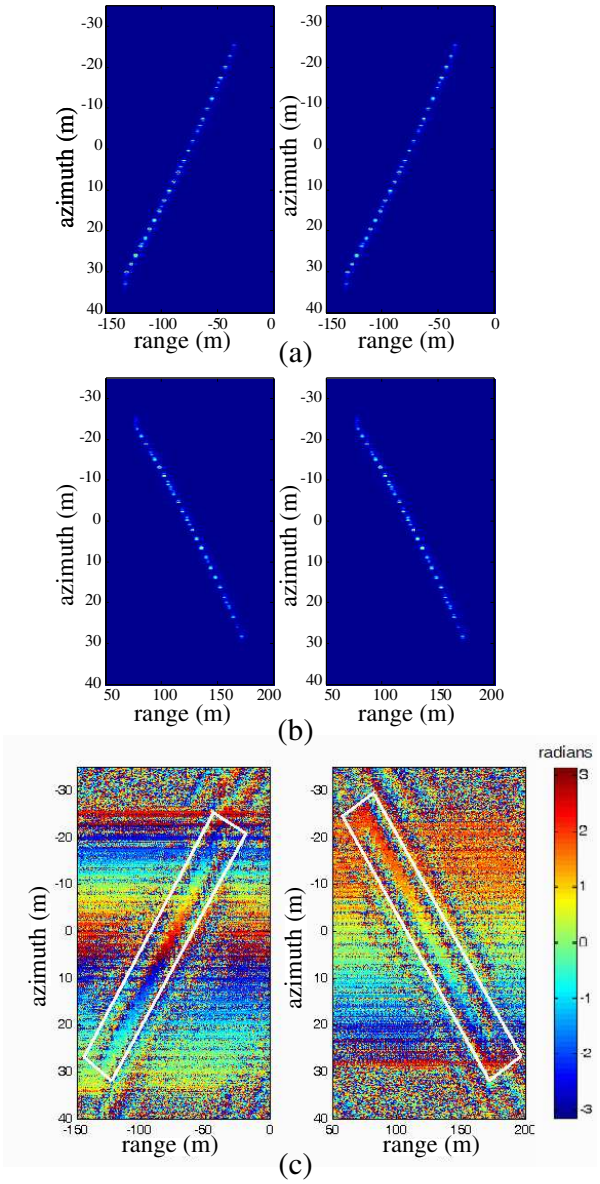

Figure 6. The coherent imaging results (HH). (a) Two channel radar images of a north-bound train. (b) Two channel radar images of a south-bound train. (c) Interferometric-phase images. The left corresponds to the north-bound train and the right corresponds to south-bound train.

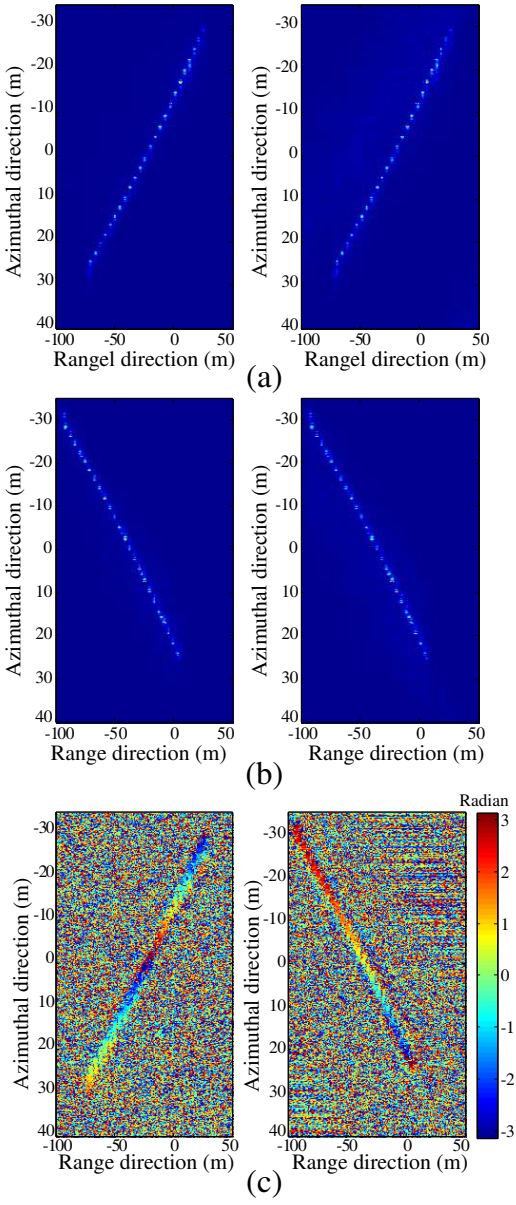

Figure 7. The incoherent imaging results (HH). (a) Two channel radar images of a north-bound train. (b) Two channel radar images of a south-bound train. (c) Interferometric-phase images. The left corresponds to the north-bound train and the right corresponds to south-bound train.

SAR image of south-bound train and the SAR image of north-bound train, one can easily find that they are vertically symmetrical, i.e., the upside-down SAR image of south-bound train is almost as same as the SAR image of north-bound train.

Both Figures 6(c) and 7(c) clearly show that the train speed is not a constant, neither for south-bound train nor for north-bound train. Because the baseline of along track interferometry is fixed, if the train speed is uniform, then the resulted interferometric phase should be a constant as well. In fact, the variation range of interferometric phase along scattering centers reflects the speed variation range. The interferometric phase of north-bound case changes much faster than that of south-bound case does. It means the north-bound case, but does not mean that the average speed of north-bound train is larger than that of south-bound train. Although the interferometric-phase images of Figure 7(c) are not as good as that of Figure 6(c) due to less SNR, the same speed information is still reflected. Let's further compare Figures 6(c) and 7(c). One can see that the interferometric-phase images of Figure 6(c) show some strong "grating lob" effect due to strong multiple scattering, but they are not shown in that of Figure 7(c). It means that multiple scattering effects can be weakened in incoherent scattering situation.

Although the interferometric-phase images reflect the speed variation very well, we still cannot judge whether the train accelerates or decelerates. In the next section, we shall apply Short-Time Frequency Transform (STFT) to the azimuthal signals along different range bins so as to better know how the speeds change for both south-bound and north-bound trains.

Figure 8 shows the amplitude images of HH and HV polarizations and their interferometric-phase image, Figure 9 shows the amplitude images of VV and VH polarizations and their interferometric-phase image, all in coherent case. By comparing these amplitude images, one can see that the scattering of VV polarization is about 24 dB stronger than that of VH polarization, and the scattering of HH polarization is about 17 dB stronger than that of HV polarization. The scattering of HH polarization is a little stronger than that of VV scattering. In principle, the scattering of HV should be as large as that of VH; however the former is about 3 dB smaller than the later as seen from Figures 8 and 9. Our explanation is that the view angles were slightly different when we changed the polarization of horn antenna from H to V during experiment. By comparing the interferometric phases, one can see that the interferometric phase of HH-HV is better than that of VV-VH, but both of them are not as good as that of HH-HH neither for coherent case nor for incoherent case, because the signals

of HV and VH are much weaker than that of HH or VV.

4.2. Scattering Analysis

In order to analyze and illustrate the scattering characteristics of the train easily, we give an optical photo of the train in Figure 10, from which one can see that the train has six compartments, and two of them are locomotives. Each compartment has four similar bigger doors and three similar bigger windows. Each of the central compartments has two similar smaller windows, and each locomotive has one similar smaller door with smaller windows. So the train totally has 24 similar bigger doors, 18 similar bigger windows, 8 similar smaller windows, 2 similar smaller doors with smaller windows.

From the above amplitude images we can see that there are 24 stronger scattering centers, and after every 4 stronger points, there is 1 weaker point. Obviously the 24 stronger scattering points correspond to the 24 bigger doors, and the weaker points between every 4 stronger points correspond to the connection of compartments (there are 5 such points). Because the train body is made of metal material and the viewing angle as large as 30°, the back scattering from train body is very weak compared with that from doors. As for the windows, part of the incident wave is forward reflected by the flat window glasses, and part of the incident wave penetrates through the glasses and gets into the compartments, so very weak backscattering is resulted. For the

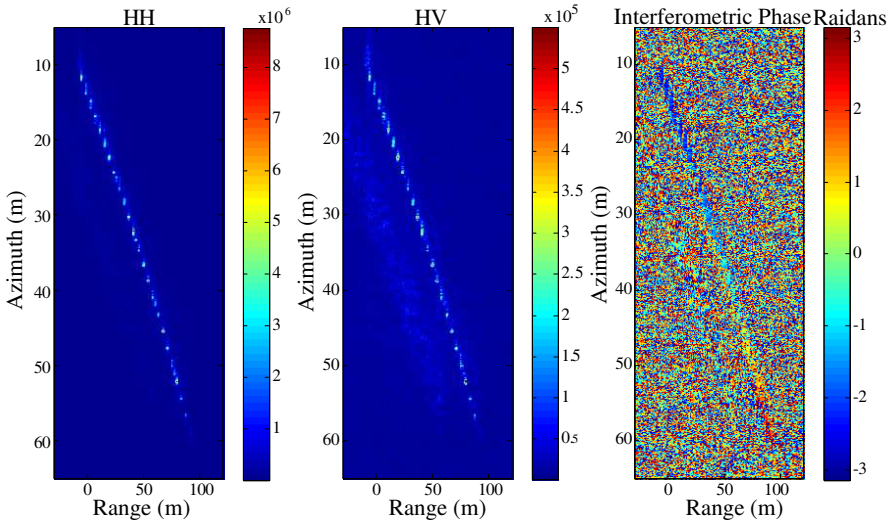

Figure 8. The amplitude images of HH and HV polarizations and their interferometric-phase image (south-bound train).

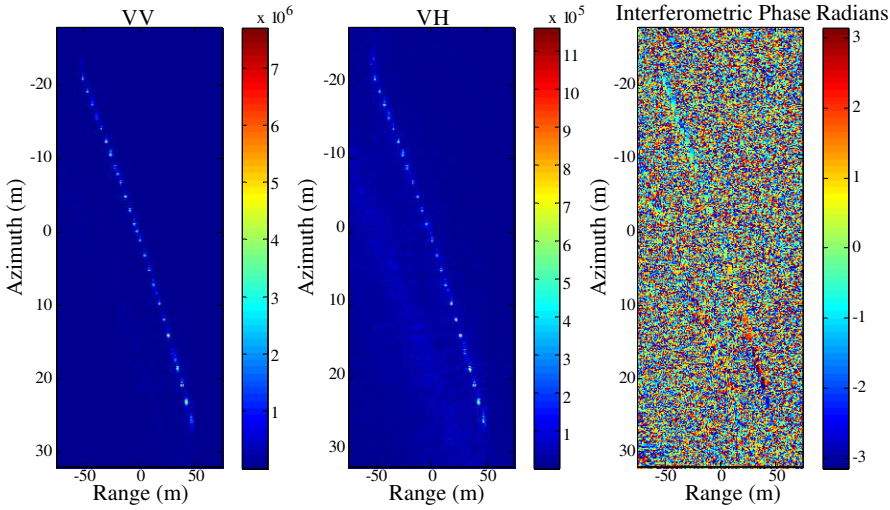

Figure 9. The amplitude images of VV and VH polarizations and their interferometric-phase image (south-bound train).

south-bound case, the scattering from the front locomotive is visible, and for the north-bound case the scattering from the back locomotive is visible. By comparing HH and HV images or VV and VH images, one can find that the scattering from connections of compartments in cross-pol case is much weaker than that in co-pol case.

5. TIME-FREQUENCY ANALYSIS OF AZIMUTHAL SIGNALS

In this section, the application of Short Time Fourier Transformation (STFT) [22–25] to azimuthal signals is conducted for comparing the speed variations of both south-bound and north-bound trains and for better knowing the speeds of the train. Two kinds of azimuthal signals are selected for analysis, i.e., for the first kind, the azimuthal signals are selected along the slow time (corresponding to pulse number) at fixed range bin (gate) as shown in Figure 5, and for the second kind, the azimuthal signals are selected corresponding to different part of the train after range cell migration correction (RCMC) performed to the range compressed signals as shown in Figure 6. Figure 11 and Figure 12 show the spectrograms of $|\mathrm{STFT}(t,\omega)|$ for the south-bound train and the north-bound train, respectively. Figure 11(a) shows the IDFs for near range bin of 412, middle range bin of 452 and far range bin of 492. Figure 11(b) shows the IDFs for the train head, middle,

Figure 10. The optical photo of the train.

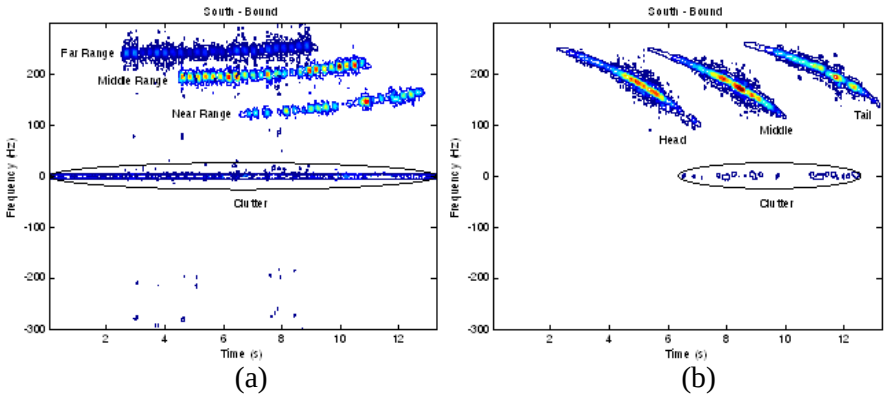

Figure 11. The IDFs versus slow time for south-bound case. (a) The IDFs versus slow time at near range (310), middle range (350) and far range (390). (b) The IDFs versus slow time for the train head, middle, and tail.

and tail. Figure 12(a) shows the IDFs for near range bin of 310, middle range bin of 350, and far range bin of 390. Figure 12(b) shows the IDFs for the train head, middle, and tail.

We know that the speed information of the train can be inferred from the IDFs, the larger the absolute of Doppler frequencies the larger the radial speed between the train and the radar for a fixed viewing angle. Figure 11(a) indicates that when the train moved into the radar beam at far range bin, the acceleration was small but positive, and when the train moved out of the beam the acceleration became larger than the beginning. Similar speed variation information is also shown in Figure 11(b): the speed of the train middle is a little bit larger than that of the train head while the speed of the train tail is remarkably

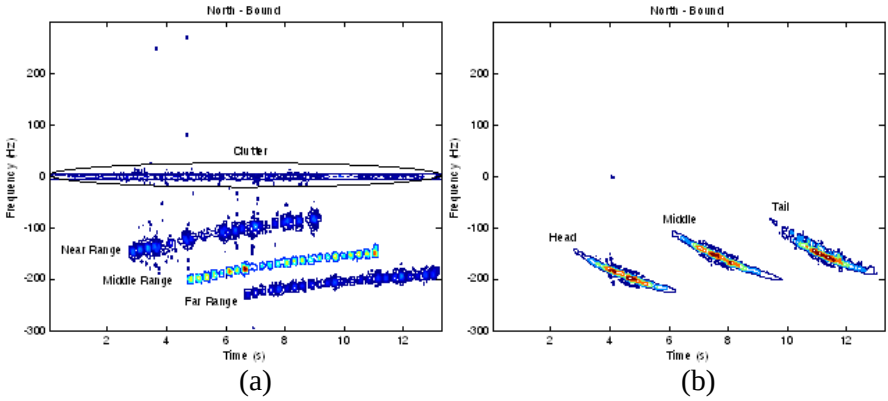

Figure 12. The IDFs versus slow time for north-bound case. (a) The IDFs versus slow time at near range (412), middle range (452) and far range (492). (b) The IDFs versus slow time for the train head, middle, and tail.

larger than that of the train head and train middle. When one compare the absolute values of the IDFs at different range bins, they look like to be contradictive with each other: now that the train is in acceleration from moving into the beam until moving out of the beam, why the absolute speed at end time (with Doppler frequencies below 200 Hz) is smaller than that at the begin time (with Doppler frequencies above 200 Hz)? The "contradiction" is also shown in Figure 11(b), where the speed variation trends of train head, train middle, and train tail are all from larger to smaller. How can the speed of the train tail be larger than that of the train head? If we check the imaging geometry as shown in Figure 2, then it can be explained as due to the viewing angle of radar relative to the moving direction of the train that changes from larger one to smaller one (variation range is about 3 dB beamwidth of antenna, i.e., about 10° or larger). We know $\cos(\theta + 10^\circ) < \cos\theta$ when $(\theta + 10^\circ) < 90^\circ$, which means that the projection speed at near range gate could be smaller than that at far range gate even if the actual speed is larger at near range gate than that at far range gate. In the future we shall further investigate the speed variation issue much more quantitatively.

Similarly, we can get the speed variation information for the north-bound case. Figure 12(a) indicates that when the train moved into the radar beam at near range gate, the acceleration was large but negative, and when the train moved out of the beam the absolute acceleration became smaller than the beginning, so the train moved at decreasing speed as also shown in Figure 12(b). The "contradiction" between

the speed variation trend and the apparent absolute speed can also be explained similarly as done for the south-bound case.

If one further compare Figures 11(a) and 12(a), it can be very easy to find that the average speeds (i.e., average Doppler frequencies) at far range, middle range and near range in south-bound case are all larger than that in north-bound case. One can also infer the speed variation from the slopes of "IDFs versus time" at far range, middle range and near range, i.e., the larger the slope the larger the speed variation. Obviously, the slopes in north-bound case is larger than that in south-bound case, i.e., the speed variation of north-band train is larger than that of south-bound train, which is in accordance with that shown in interferometric-phase.

6. CONCLUSION

Ground moving target imaging and scattering experiments were carried out on a light railway train by a ground Ku-band radar system with two receiving channels, and both coherent and incoherent scattering results were obtained, as well as co-pol and cross-pol interferometric results. SAR signal model and RD algorithm are applied to reconstructing radar images. Only the doors and connections of compartments are visible in SAR images due to large viewing angle. The obtained interferometric-phase images distinctly show that the south-bound train traveled at a relative fast changing speed and that the north-bound train traveled at a relative slowly changing speed. STFT is applied to the azimuthal signals to get IDFs for better knowing the speed variation. The results clearly show that the south-bound train traveled at accelerating speed while the north-bound train traveled at decelerating speed. Results also show that in incoherent imaging case, the transmitter that used USCO needs not to be phase-synchronized to the receiver that used USCO if there is a very small frequency difference between them, and both of them are ultra-stable. In the future work, we will further exploit the interferometric-phase images with the TFA results and try to infer the exact viewing angle so as to get the exact velocity of the train.

REFERENCES

1. Perry, R. P., R. C. Dipietro, and R. L. Fante, "SAR imaging of moving targets," *IEEE Trans. Aerosp. Electron. Syst.*, Vol. 35, No. 1, 188–200, 1999.
2. Mao, X. H., D. Y. Zhu, L. Ding, and Z. D. Zhu, "Comparative study of RMA and PFA on their responses to moving target," *Progress In Electromagnetics Research*, Vol. 110, 103–124, 2010.

3. Zhou, F., R. Wu, M. Xing, and Z. Bao, "Approach for single channel SAR ground moving target imaging and motion parameter estimation," *IET Radar, Sonar & Navigation*, Vol. 1, 59–66, 2007.
4. Zhu, D., Y. Li, and Z. Zhu, "A keystone transform without interpolation for SAR ground moving-target imaging," *IEEE Trans. Geoscience & Remote Sensing Letters*, Vol. 4, No. 1, 18–22, 2007.
5. Graham, L. C., "Synthetic interferometric radar for topographic mapping," *IEEE Proceedings*, Vol. 62, 763–768, 1974.
6. Wu, B.-I., M. C. Yeung, Y. Hara, and J. A. Kong, "Insar height inversion by using 3-D phase projection with multiple baselines," *Progress In Electromagnetics Research*, Vol. 91, 173–193, 2009.
7. Li, S., H. Xu, and L. Zhang, "An advanced DSS-SAR InSAR terrain height estimation approach based on baseline decoupling," *Progress In Electromagnetics Research*, Vol. 119, 207–224, 2011.
8. Tian, B., D. Y. Zhu, and Z. D. Zhu, "A novel moving target detection approach for dual-channel SAR system," *Progress In Electromagnetics Research*, Vol. 115, 191–206, 2011.
9. Fan, C.-Y., X.-T. Huang, T. Jin, J.-G. Yang, and D.-X. An, "Novel pre-processing techniques for coherence improving in along-track dual-channel low frequency SAR," *Progress In Electromagnetics Research*, Vol. 128, 171–193, 2012.
10. Zhang, Y., X. Zhang, et al., "Moving train imaging by ground-based Ka-band radar," *Loughborough Antenna and Propagation Conference (LAPC)*, 413–416, Loughborough, UK, Nov. 16–18, 2009.
11. Zhang, X., W. Zhai and Y. Zhang, "A prototype for stepped-frequency SAR dechirp imaging system and experimental verification," *Asia-Pacific Microwave Conference (APMC)*, Singapore, Dec. 7–10, 2009.
12. Zhang, Y., X. Zhang, W. Zhai, X. Shi, and X. Gu, "Radar imaging and electromagnetic scattering analysis for moving train by ku-band ground-based interferometric radar," *Asia-Pacific Microwave Conference (APMC)*, Singapore, Dec. 7–10, 2009.
13. Zhang, Y., Y. Deng, W. Zhai, X. Zhang, and J. Jiang, "Time-frequency processing and analysis of radar imaging experiment data for a moving train," *The 7th IASTED International Conference on Antennas, Radar and Wave Propagation (ARP)*, Cambridge, Massachusetts, USA, Nov. 1–3, 2010.
14. Yu, L. and Y. Zhang, "Application of the fractional fourier

transform to moving train imaging," *Progress In Electromagnetics Research M*, Vol. 19, 13–23, 2011.

15. Park, J.-I. and K.-T. Kim, "A comparative study on ISAR imaging algorithms for radar target identification," *Progress In Electromagnetics Research*, Vol. 108, 155–175, 2010.
16. Burkholder, R. J., I. J. Gupta, and J. T. Johnson, "Comparison of monostatic and bistatic radar images," *IEEE Antennas and Propagation Magazine*, Vol. 45, No. 3, 41–50, 2003.
17. Calvo-Gallego, J. and F. Pérez-Martínez, "Simple traffic surveillance system based on range-doppler radar images," *Progress In Electromagnetics Research*, Vol. 125, 343–364, 2012.
18. Woo, J.-C., B.-G. Lim, and Y.-S. Kim, "Modification of the recursive sidelobe minimization technique for the range-doppler algorithm of SAR imaging," *Journal of Electromagnetic Waves and Applications*, Vol. 25, No. 13, 1783–1794, 2011.
19. Koo, V. C., Y. K. Chan, and H. T. Chuah, "Multiple phase difference method for real-time SAR autofocus," *Journal of Electromagnetic Waves and Applications*, Vol. 20, No. 3, 375–388, 2006.
20. Koo, V. C., Y. K. Chan, and H. T. Chuah, "A new autofocus based on sub-aperture approach," *Journal of Electromagnetic Waves and Applications*, Vol. 19, No. 11, 1547–1561, 2005.
21. Koo, V. C., T. S. Lim, M. V. C. Rao, and H. T. Chuah, "A GA-based autofocus technique for correcting high-frequency sar phase error," *Journal of Electromagnetic Waves and Applications*, Vol. 18, No. 6, 781–795, 2004.
22. Han, S.-K., H.-T. Kim, S.-H. Park, and K.-T. Kim, "Efficient radar target recognition using a combination of range profile and time-frequency analysis," *Progress In Electromagnetics Research*, Vol. 108, 131–140, 2010.
23. Nawab, H. and T. F. Quatieri, "Short-time fourier transform," *Advanced Topics in Signal Processing*, J. S. Lim, and A. V. Oppenheim, Editors, Chapter 6, 289–337, Prentice Hall, New Jersey, 1988.
24. Son, J. S., G. Thomas, and B. C. Flores, *Range-Doppler Radar Imaging and Motion Compensation*, Artech Hourse, Norwood, 2001.
25. Chen, V. C. and H. Ling, *Time-Frequency Transforms for Radar Imaging and Signal Analysis*, Artech Hourse, Norwood, 2002.